

On-chip Fourier transform spectrometer on silicon-on-sapphire

ELHAM HEIDARI,^{1,*} XIAOCHUAN XU,^{1,2} CHI-JUI CHUNG,¹ AND RAY T. CHEN^{1,3}

¹Microelectronics Research Center, Electrical and Computer Engineering Department, University of Texas at Austin, Austin, Texas 78758, USA

²Omega Optics Inc., Austin, Texas 78757, USA

³e-mail: chenrt@austin.utexas.edu

*Corresponding author: e.heidari@utexas.edu

Received 18 March 2019; accepted 30 April 2019; posted 8 May 2019 (Doc. ID 362586); published 30 May 2019

We designed and experimentally demonstrated an on-chip Fourier transform spectrometer on silicon-on-sapphire. The spectrometer comprises an array of twelve Mach-Zehnder interferometers (MZIs) with linearly increasing optical path delays between MZI arms. The propagation loss of 5.2 dB/cm has been experimentally observed for the strip waveguides. The retrieval of an optical spectrum is demonstrated with an inter-band cascade laser centered at 3.3 μm . The resolution is better than 10 cm^{-1} . © 2019 Optical Society of America

<https://doi.org/10.1364/OL.44.002883>

Optical spectroscopy is an indispensable tool in numerous areas including optical communication, sensing, material analysis, and medical applications. The advance of the on-chip spectrometer empowers compact, low-cost spectroscopy operating for portable sensing and enhancement of lab-on-a-chip [1–4]. Since the optical path length limits the spectral resolution, particularly high performance spectrometers, which rely on dispersive components, are inevitably bulky and expensive [5].

Fourier transform spectroscopy (FTS) is a technique that measures the spectrum with the interference of light instead of dispersion [6]. An infrared spectrum represents a fingerprint of a material with absorption peaks that corresponds to the frequencies of vibrations between the bonds of the atoms making up the material [7]. Compared to dispersive optics or filter-based spectroscopy approaches, the primary advantages of FTS include high optical throughput, thereby larger signal-to-noise ratio, compact size, and high sensitivity [8–12]. A typical FTS is composed of an infrared source, a Michelson interferometer (MI), a detector, and a He-Ne laser for alignment and positioning. The whole system is bulky, heavy, and sensitive to environmental fluctuations (vibration, etc.). These disadvantages make it an unsuitable method for many resource-restrained applications, such as airborne and space borne applications. Integrated photonics provides a potential solution. Several attempts have been reported in recent years, but most of them are in the near-infrared wavelength range, which corresponds to the overtone of molecule vibration, and therefore lacks

sensitivity and specificity [13–15]. In this paper, we report the experimental demonstration of an on-chip FTS at the mid-infrared wavelength range, which shows the potential to achieve high resolution and wide wavelength range at on-chip FTS.

Typical benchtop FTS is based on the MI. The path length difference is generated by moving the mirror in one arm of the interferometer [1]. This configuration cannot be easily implemented on-chip, as physically changing the position of a component on-chip is challenging. Although micro-electro-mechanic systems (MEMS) can move components, the moving distance is very limited, and the operation voltage is high [16–18]. The proposed on-chip FTS is shown in Figure 1(a). The FTS is formed by an array of twelve Mach-Zehnder interferometers (MZIs) with linearly increased path length difference ΔL_i ($i = 1, 2, \dots, 12$). The spectrum can be retrieved with the interferograms from the twelve channels through discrete Fourier

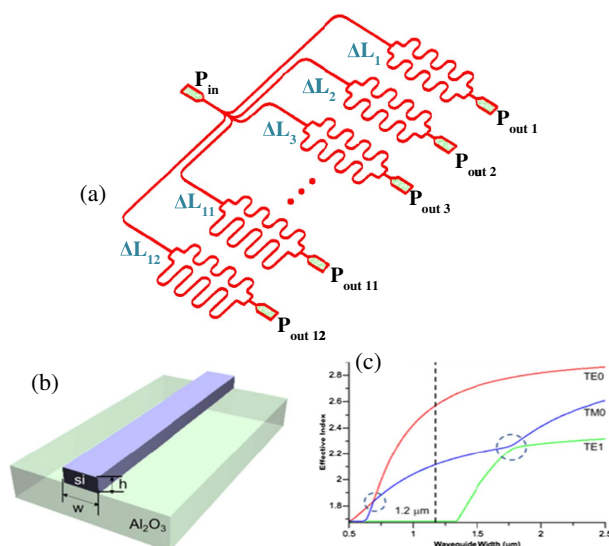


Fig. 1. (a) Schematic structure of the designed MZI array. (b) Schematic of the strip waveguide ($b = 600$ nm). (c) Effective index of TE_0 , TM_0 , and TE_1 when waveguide width varies from 0.5 to 2.5 μm . Dashed line represents $w = 1.2$ μm . Circles represent the anti-crossing point.

transform, as shown by Eq. (1) [19]. The phase change is converted into an intensity change using interferometric schemes. The detected intensity is a cosine function of the path differences, which is the fundamental relation in the FTS:

$$P^{\text{in}}(\bar{\sigma}) = \Delta x P^{\text{in}} + 2\Delta x \sum_{i=1}^N F(x_i) \cos 2\pi\bar{\sigma}x_i. \quad (1)$$

Here, σ is the wavenumber, and $\bar{\sigma} = \sigma - \sigma_{\text{min}}$ is the shifted wavenumber, where σ_{min} represents the minimum wavenumber. x_i is defined as $x_i = n_{\text{eff}}\Delta L_i$. Δx represents the increment of the path length difference between the adjacent two MZIs. n_{eff} is the effective index of the strip waveguide, and ΔL_i is the physical length difference. P^{in} represents the total power of the input light source. The interference term $F(x_i)$ is defined as [19]

$$F(x_i) = \frac{1}{B_s} (2P_i^{\text{out}} - A_s P^{\text{in}}). \quad (2)$$

P_i^{out} denotes the output power of the i th MZI. The equation is derived based on the assumption that the coefficients A_s and B_s are wavelength independent [19]. These coefficients comprise the coupling and loss coefficients of the MZI components, respectively. The wavenumber resolution $\delta\sigma$ of the spectrometer is determined by the maximum interferometric delay Δx_{max} which is the delay corresponding to the most unbalanced MZI in the array [19]. To resolve two monochromatic signals with wavenumbers σ and $\sigma + \delta\sigma$, the respective interferograms differ by one fringe, equivalent to the interferogram phase change of 2π :

$$\Delta\varphi = 2\pi(\sigma + \delta\sigma)\Delta x_{\text{max}} - 2\pi\delta\sigma\Delta x_{\text{max}} = 2\pi. \quad (3)$$

Thus, $\delta\sigma\Delta x_{\text{max}} = \delta\sigma n_{\text{eff}}\Delta L_{\text{max}} = 1$. The maximum path delay of the arrayed MZI is, therefore,

$$n_{\text{eff}}L = \frac{1}{\delta\sigma}. \quad (4)$$

The number of discrete points N in the interferogram is determined by the Fourier sampling theorem [19]. For the spectral power non-vanishing only within the range $\Delta\sigma$, the spectrum $p^{\text{in}}(\sigma)$ is fully specified by sampling the interferogram at an interval not exceeding spectral intervals $(2\Delta\sigma)^{-1}$. In other words, the minimum number of sampling points is

$$N_{\text{min}} = 2\frac{\Delta\sigma}{\delta\sigma} = 2\frac{\Delta\lambda}{\delta\lambda}, \quad (5)$$

where $\Delta\lambda$ is the wavelength spectral range of the spectrometer. To resolve the two peaks in the emission spectrum of the inter-band cascade laser (ICL), the resolution should be better than 10 cm^{-1} , corresponding to an $n_{\text{eff}}\Delta L_{\text{max}}$ of 0.1 cm. Here, $n_{\text{eff}}\Delta L_{\text{max}} = 0.12 \text{ cm}$ is chosen to assure that the distinguishing of the two peaks can be demonstrated experimentally.

The FTS is designed based on the strip waveguide, the schematic of which is shown in Fig. 1(b). The waveguide width (w) is scanned, and the corresponding n_{eff} is plotted in Fig. 1(c). The height of the waveguide is 600 nm. In this demonstration, the waveguide width is $1.2 \mu\text{m}$ to assure a single TE mode is supported by the waveguide, corresponding to an n_{eff} of 2.643. According to Eq. (5), a minimum number of twelve MZIs is required. Thus, the path length difference increment was $\Delta L = 41 \mu\text{m}$.

The devices are fabricated on a silicon-on-sapphire (SOS) platform with a 600 nm silicon layer on a 500 μm thick

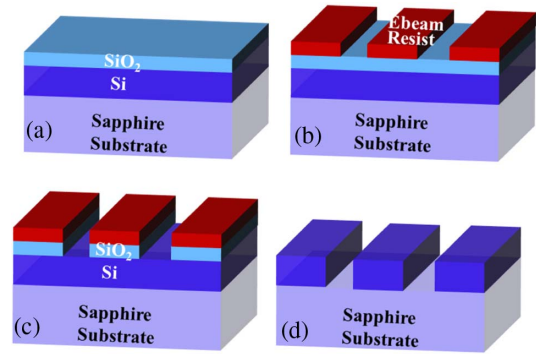


Fig. 2. Fabrication process. (a) PECVD growth of 130 nm SiO_2 as hard mask. (b) e-beam lithography. (c) Etch SiO_2 with RIE. (d) Etch Si with ICP and post-fabrication treatment with Piranha/HF.

sapphire substrate. The major fabrication steps are summarized in Fig. 2. A 130 nm silicon dioxide (SiO_2) layer is first deposited on top of the silicon layer using plasma enhanced chemical vapor deposition (PECVD) as a hard mask for the pattern transfer. All the components, including sub-wavelength grating (SWG) couplers, strip waveguides, and MZIs, are patterned in one step using the JEOL JBX-6000FS electron-beam (e-beam) lithography tool with ZEP-520A e-beam resist, followed by developing in n-Amyl acetate for 2 min, and rinsing in isopropyl alcohol. The e-beam resist pattern is next transferred to SiO_2 by reactive ion etching (RIE) using CHF_3 and O_2 at 400 V DC bias and 40 mTorr pressure. Following this, the pattern in SiO_2 is transferred to silicon by inductively coupled plasma (ICP) etch using HBr and Cl_2 at 400 W ICP power, 200 W RF power, 10 mTorr pressure, and 20 Torr He flow for backside cooling. Finally, the chip is cleaned using Piranha and followed with cycles of Piranha/HF post process treatment.

The fabricated FTS chip is shown in Fig. 3(a). A penny is put next to the chip to show the size of the chip. An optical microscopic image of the dashed area is shown in Fig. 3(b). The cross-section scanning electron microscope (SEM) image of the fabricated strip waveguide is shown in Fig. 3(c). The fabricated SWG coupler is shown in Fig. 3(d). Compared to the device at the telecommunication wavelength, e.g., 1550 nm, the feature size at $3.3 \mu\text{m}$ is much larger. Thus, the charging accumulation effect of e-beam lithography is fierce and needs to be compensated in advance to assure a precise transfer of patterns into the silicon.

To test the fabricated grating couplers and waveguides, a mid-infrared set up has been built in-house, as shown in Fig. 4. The 3.3 μm ICL from Thorlab is used as the light source, which is driven by a Thorlab laser driver and temperature controller. Aspheric lenses are used to collimate the light from the ICL and coupled into a ZrF_4 fiber. The fiber is mounted on a 10 deg wedge sitting on a high precision stage to couple light into the on-chip circuit. The light coupled out from the chip is collected by another ZrF_4 fiber. An InSb detector with responsivity of 3.73 A/W is used to capture the optical signal. To increase the signal-to-noise ratio, a locked-in amplifier is used with a chopper frequency of 300 Hz.

Grating couplers can selectively excite one of the modes and suppress others when designed properly. Coupling efficiency for different incident angles of the TE polarization slot mode

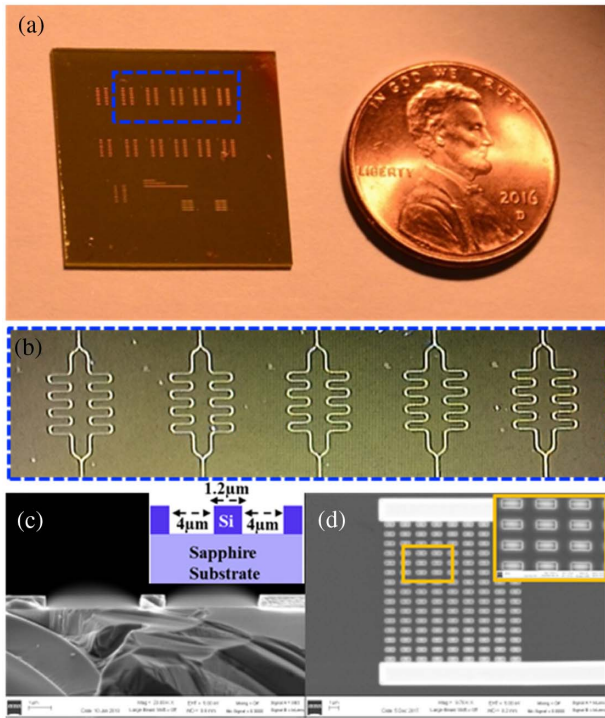


Fig. 3. (a) Fabricated FTS chip. A penny is put next to the chip to show the size. (b) Optical microscopic image of the dashed area. (c) Cross-section of the strip waveguide. The SEM image shows the trenches with 4 μm width for each side and strip waveguide with 1.2 μm width. (d) Top view of the fabricated SWG coupler. Inset: zoomed-in view of the SWG structure.

is measured and compared with the simulation results, as shown in Fig. 5(a). The maximum coupling efficiency is achieved with 14 deg incident angles, while the simulation shows the maximum coupling efficiency at 12 deg, which is observed in Fig. 5(a). Figure 5(b) shows the measured loss from five strip waveguides with lengths ranging from 2.5 to 15 mm. The error percentage of the photodetector is observed less than 1%. By performing a linear fit to the data, a propagation loss of 5.2 dB/cm is obtained for the strip waveguide. Since the maximum physical path length difference is only 0.454 mm, and the targeted resolution is not high, the loss induced errors can be ignored.

Figure 6(a) shows the output interferogram of the twelve MZIs for the measured wavelength range compared with the

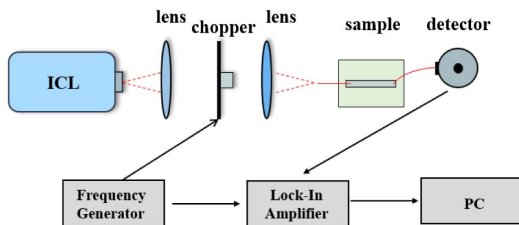


Fig. 4. Schematic of the experimental setup. Light from the ICL is collimated and coupled into the ZrF_4 fiber. SWG couplers are leveraged to couple light into and out from the MZIs. The output light is collected by the InSb detector.

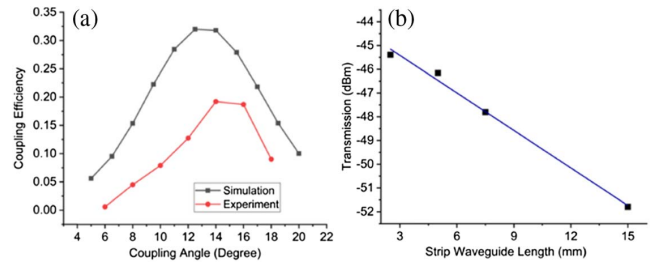


Fig. 5. (a) Grating coupler's coupling efficiency as a function of coupling angle. (b) Measured loss of strip waveguides fabricated on SOS operating at 3.3 μm wavelength.

simulation results. Since Δx_{max} is small, the dispersion difference between the two arms of the MZIs is negligible. Besides, the bandwidth of the grating coupler is large compared to the wavelength spectral range of the spectrometer, and the effect of wavelength dependent coupling efficiency is small. Therefore, the assumption that A_s and B_s are wavelength independent is valid in this demonstration. Reasonable agreement between measured output power and simulation results are observed and are shown in Fig. 6(a). The discrepancies are primarily caused by the fabrication induced phase errors. The retrieved spectrum is shown in Fig. 6(b). The red curve is the spectrum of the ICL obtained from a benchtop FTS system with 2 cm^{-1} resolution. The circles are obtained by applying Eq. (1) on the interferogram obtained from the twelve MZIs. The blue curve is the cubic fitting of the data. The two peaks of the ICL spectrum are successfully distinguished by the on-chip FTS. Higher resolution can be achieved through increasing the number and

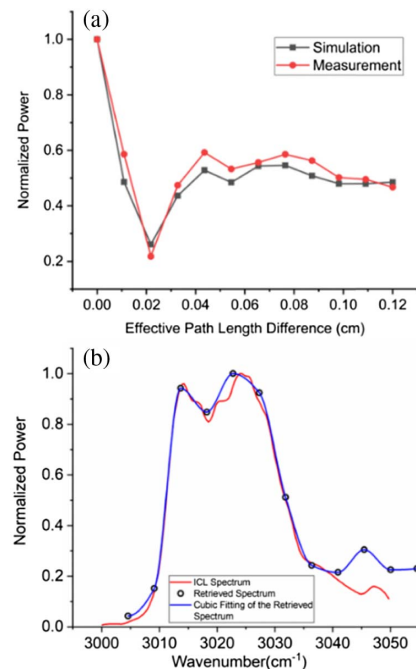


Fig. 6. (a) Simulation and measurement results (power-effective path length difference) obtained for the output power of the MZI array. (b) Power versus wavenumber results of the measured Mach-Zehnder waveguides that show that the output could detect the input spectrum most clearly.

the maximum path length difference of the MZIs. However, when the path length difference becomes large, the dispersion and the propagation loss must be taken into consideration. Thus, Eq. (1) needs to be revised to include these factors. In this case, A_s and B_s become wavelength dependent.

In summary, we demonstrated an on-chip FTS on a SOS platform with a resolution better than 10 cm^{-1} . The retrieval of the ICL spectrum is demonstrated. The resolution can be further improved by increasing the integration density or employing slow light effects. Besides, advanced retrieval methods, such as the compressed sensing spectroscopy, can be used to reduce the number of MZIs [20].

FUNDING

National Aeronautics and Space Administration (NASA) SBIR Phase I (Contract #: NNX17CM40P).

REFERENCES

1. D. A. L. Smith, *Applied Infrared Spectroscopy* (Wiley-Interscience, 1979).
2. R. F. Wolffenbuttel, *IEEE Trans. Instrum. Meas.* **53**, 197 (2004).
3. P. Cheben, I. Powell, S. Janz, and D.-X. Xu, *Opt. Lett.* **30**, 1824 (2005).
4. B. I. Akca, B. Považay, A. Alex, K. Wörhoff, R. M. de Ridder, W. Drexler, and M. Pollnau, *Opt. Express* **21**, 16648 (2013).
5. M. Khorasaninejad, A. Y. Zhu, C. R. Cames, W. T. Chen, J. Oh, I. Mishra, R. C. Devlin, and F. Capasso, *Nano Lett.* **16**, 7229 (2016).
6. M.-L. Junttila, J. Kauppinen, and E. Ikonen, *J. Opt. Soc. Am. A* **8**, 1457 (1991).
7. R. Baets, A. Z. Subramanian, A. Dhakal, Sh. K. Selvaraja, K. Komorowska, F. Peyskens, E. Ryckeboer, N. Yebo, G. Roelkens, and N. L. Thomas, *Proc. SPIE* **8627**, 86270I (2013).
8. B. C. Smith, *Fundamentals of Fourier Transform Infrared Spectroscopy*, 2nd ed. (2011).
9. P. R. Griffiths, *Appl. Spectrosc.* **71**, 329 (2017).
10. A. Rahim, E. Ryckeboer, A. Z. Subramanian, S. Clemmen, B. Kuyken, A. Dhakal, A. Raza, A. Hermans, M. Muneeb, S. Dhoore, Y. Li, U. Dave, P. Bienstman, N. L. Thomas, G. Roelkens, D. V. Thourhout, Ph. Helin, S. Severi, X. Rottenberg, and R. Baets, *J. Lightwave Technol.* **35**, 639 (2017).
11. G. Reich, *Adv. Drug Delivery Rev.* **57**, 1109 (2005).
12. P. D. Heyn, J. D. Coster, P. Verheyen, G. Lepage, M. Pantouvaki, P. Absil, W. Bogaerts, J. V. Campenhout, and D. V. Thourhout, *J. Lightwave Technol.* **31**, 3085 (2013).
13. N. K. Fontaine, K. Okamoto, T. Su, and S. J. B. Yoo, *Opt. Lett.* **36**, 3124 (2011).
14. P. J. Bock, P. Cheben, A. V. Velasco, J. H. Schmid, A. Delage, M. Florjanczyk, J. Lapointe, D. Xu, M. Vachon, S. Janz, and M. L. Calvo, *Laser Photon. Rev.* **7**, L67 (2013).
15. A. V. Velasco, P. Cheben, P. Bock, A. Delage, J. H. Schmid, J. Lapointe, S. Janz, M. L. Calvo, D. Xu, M. Florjanczyk, and M. Vachon, *Opt. Lett.* **38**, 706 (2013).
16. K. Yu, N. Park, D. Lee, and O. Solgaard, *IEEE Sensors* (2006), p. 412.
17. H. Omran, M. Medhat, B. Mortada, B. Saadany, and D. Khalil, *IEEE J. Quantum Electron.* **48**, 244 (2012).
18. T. Scharfa, D. Brianda, S. Bühlerb, O. Manzardob, H. P. Herziga, and N. F. de Rooija, *Procedia Chem.* **1**, 1379 (2009).
19. M. Florjanczyk, P. Cheben, S. Janz, A. Scott, B. Solheim, and D. Xu, *Opt. Express* **15**, 18176 (2007).
20. H. Podmore, A. Scott, P. Cheben, A. V. Velasco, J. H. Schmid, M. Vachon, and R. Lee, *Opt. Lett.* **42**, 1440 (2017).